Terr. Atmos. Ocean. Sci., Vol. 28, No. 5, 693-701, October 2017 doi: 10.3319/TAO.2016.12.28.01

3D Vs ambient noise tomography of the 2016 M_w 6.4 Meinong Earthquake source region in Taiwan

Hao Kuo-Chen[1, *], Kai-Xun Chen[2], Wei-Fang Sun[3], Chun-Wei Ho[1, 4], Yuan-Hsi Lee[5], Zhuo-Kang Guan[1], Chu-Chun Kang[1], and Wen-Yen Chang[3]

[1] *Department of Earth Sciences, National Central University, Taoyuan City, Taiwan*
[2] *Department of Geosciences, National Taiwan University, Taipei City, Taiwan*
[3] *Department of Natural Resources and Environmental Studies, National Dong Hwa University, Hualien, Taiwan*
[4] *Seismological Center, Central Weather Bureau, Taipei City, Taiwan*
[5] *Department of Earth and Environmental Sciences, National Chung Cheng University, Chiayi County, Taiwan*

Article history:
Received 26 September 2016
Revised 14 December 2016
Accepted 28 December 2016

Keywords:
Meinong earthquake, Ambient noise tomography, Gutingkeng Formation, Dense seismic array

Citation:
Kuo-Chen, H., K.-X. Chen, W.-F. Sun, C.-W. Ho, Y.-H. Lee, Z.-K. Guan, C.-C. Kang, and W.-Y. Chang, 2017: 3D Vs ambient noise tomography of the 2016 M_w 6.4 Meinong Earthquake source region in Taiwan. Terr. Atmos. Ocean. Sci., 28, 693-701, doi: 10.3319/TAO.2016.12.28.01

ABSTRACT

M_w 6.4 Meinong earthquake occurred on 6 February 2016 in southern Taiwan, resulting in more than one hundred casualties and several collapsed buildings. The aftershocks occurred mostly at mid-to-lower crustal depths (10 - 30 km), related to a blind fault system. However, several centimeters of cosesimic surface uplift within the Liushuang, Erhchungli, and GutingKeng Formations, composed mainly of mudstone, was recorded from the InSAR results. The uplifted pattern is similar to that of GPS and leveling data from 2000 - 2010, which indicates the deformation is accomplished by creeping due to the shallow mudstone structure related to mud diapir. Previous studies have shown limited information about the shallow structure in this region due to few deployed seismic stations. We deployed 36 temporary seismic stations (~5 km spacing) in this study around one month after the main shock to obtain a 3-D shear wave shallow crustal velocity structure using ambient noise tomography. The reliable periods of group and phase velocities from Rayleigh waves were 0.6 - 5 s, corresponding to around 0 - 5 km at depths. As a result, the low S-wave pattern speeds at 0 - 4 km depths correspond to the uplift region from both InSAR data for the coseismic period and GPS and leveling data for the interseismic period. The results from this study are compatible with the reflected seismic profile. The results show that with dense seismic array deployment we can obtain high subsurface image resolution to link the relationship between the surface observations to the subsurface structures.

1. INTRODUCTION

The M_w 6.4 Meinong earthquake occurred on 6 February 2016 in southern Taiwan resulting in 117 casualties and several collapsed buildings. The focal depth of this event is 14.6 km without observed surface ruptures, which indicates a blind fault system. The focal mechanisms from different methods all show thrust faulting with a strike-slip component (Fig. 1a), but the distribution of aftershocks does not show a simple fault system, which may indicate the complexity of the pre-existed fault systems (Fig. 2). It is also interesting to note that the largest ground shaking and damage were reported ~30 km away from the epicenter in the northwestern direction based on the official Central Weather Bureau report in Taiwan (Fig. 1b). Conversely, in the region around the epicenter, little damage was reported for buildings with smaller ground shaking.

Although there was no surface rupture observed in the field, the InSAR results show a narrow coseismic uplift of only several centimeters west of the epicenter and a small subsidence around the main shock region (Huang et al. 2016) (Fig. 2a). However, most of aftershocks are located below 10 km depth, which are not directly associated with the surface deformation (Figs. 2b and c). The depths of the aftershocks beneath the uplift region all occurred within the lower crustal depth (20 - 30 km) (Fig. 2b). The subsurface

* *Corresponding author*
E-mail: kuochen@ncu.edu.tw

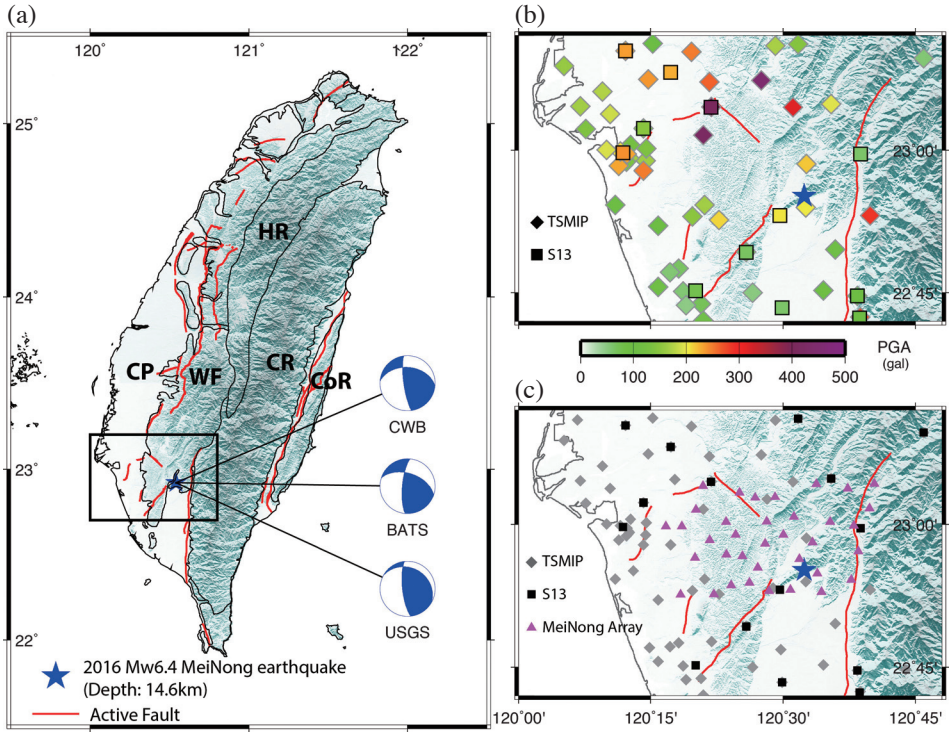

Fig. 1. (a) Geological backgrounds of Taiwan and focal mechanisms of the Meinong earthquake from the Central Weather Bureau (CWB), Broadband Array in Taiwan for Seismology (BATS), and United States Geological Survey (USGS). Abbreviations: CP: Coastal Plain; WF: Western Foothills; HR: Hsuehshan Range; CR: Central Range; CoR: Coastal Range. (b) Peak Ground Acceleration (PGA) during the Meinong earthquake. (c) Permanent (TSMIP and S13) and temporary (Meinong array) seismic networks deployed in southwestern Taiwan. (Color online only)

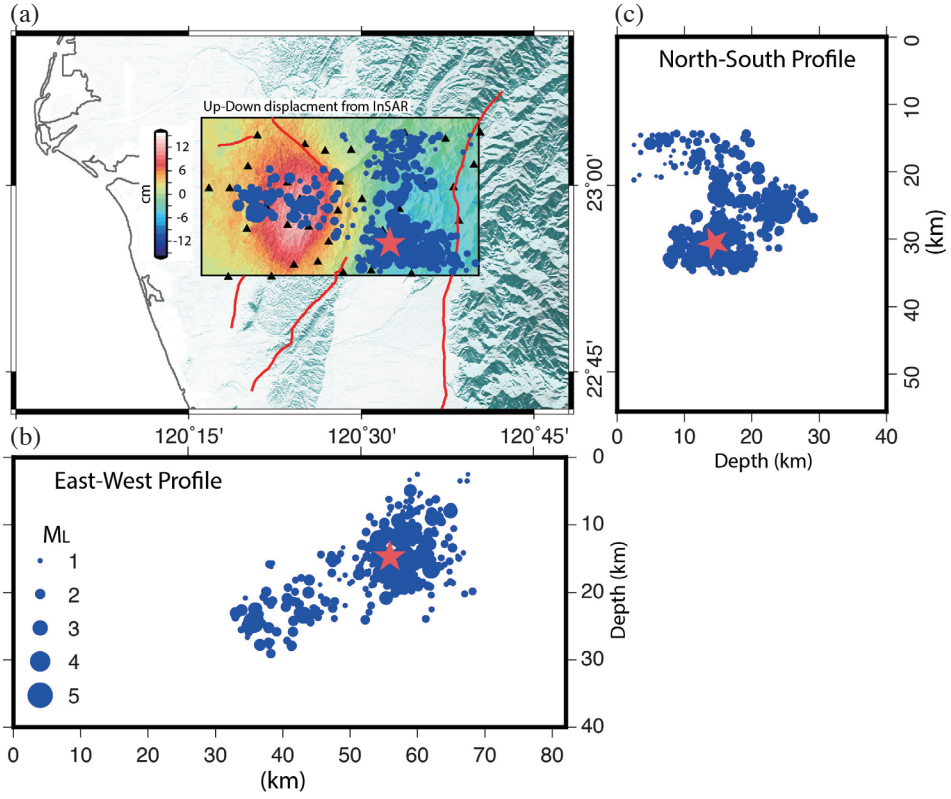

Fig. 2. The vertical coseismic displacement from InSAR results (Huang et al. 2016) and aftershocks from 10 February to 14 March 2016 during the temporary seismic array deployment. (a) Map view of Meinong earthquake sequence and the vertical coseismic displacement from InSAR. (b) and (c) vertical profiles of Meinong earthquake sequence. Red star: main shock. Blue circle: aftershocks. (Color online only)

structure in this region could be highly heterogeneous to correspond to the surface deformation. Unfortunately, due to few seismic stations deployed in this region, the 3-D high-resolution shallow subsurface images are difficult to obtain from previous studies (e.g., Kuo-Chen et al. 2012; Huang et al. 2014) (Fig. 1c). We deployed 36 temporary stations in this study for one month, three days after the main shock to obtain 3D high-resolution Vs tomography imagery from the ambient Rayleigh wave tomography. The results show that a low velocity zone (at ~0 - 2 km depths) was observed directly beneath the most uplift coseismic deformation region from the InSAR results.

2. GEOLOGICAL BACKGROUNDS

The geological structures of Taiwan orogen are the results of the arc-continental collision between the Eurasian plate and Philippine Sea plate. They can be divided into five geological units (Fig. 1a). We focus only on the geological structures in southwestern Taiwan in this study, which are involved in two geological units, the Coastal Plain (CP), and the Western Foothills (WF). The Coastal Plain (CP) is composed of sediments, which is the present-day foreland basin. The Western Foothills (WF) is composed of accreted and deformed sediments in the foreland basin (Ho 1986). We focus on the Liushuang Formation (Pls), Erhchungchi Formation (Pec), and Gutingkeng Formation (Pgtk) in the Western Foothills (Fig. 3). The Gutingkeng Formation (Pgtk) is more than 5000 m thick, which can be separated into Lower and Upper Formation. The Lower Gutingkeng Formation consists of thick mudstone with thin layers of fine-grained sandstone, deposited in bathyal depth (Teng 1987). The Upper Gutingkeng Formation is mudstone interbeded with fine to coarse grain sandstone. The Erhchungchi Formation (Pec) is shallow marine sandstone with ca. 1000 m thickness. The late Pleistocene Liushuang Formation (Pls) is comprised of loose sandstone interbeded with a thin conglomerate layer deposited in coastal to fluvial environments. The Lungchuan Fault (LCNF) is an east-dipping reverse fault with ~N-S strike in the northern part and 30°N - 40°E in the southern part (Fig. 3b).

3. DATA AND ANALYSIS

We used the ambient-noise Rayleigh wave dispersion to investigate the three-dimensional S-wave velocity of the Meinong earthquake source region from a temporary seismic array. There were 36 stations (Texan data logger with one Vertical 4.5 Hz geophone) with ~5 km spacing deployed from 10 February to 14 March 2016. The seismic array distribution was designed to fill in the gaps in the permanent seismic station network in the Meinong earthquake source region (Fig. 1c). The methodology for data processing and the Vs tomography inversion can be divided into five main

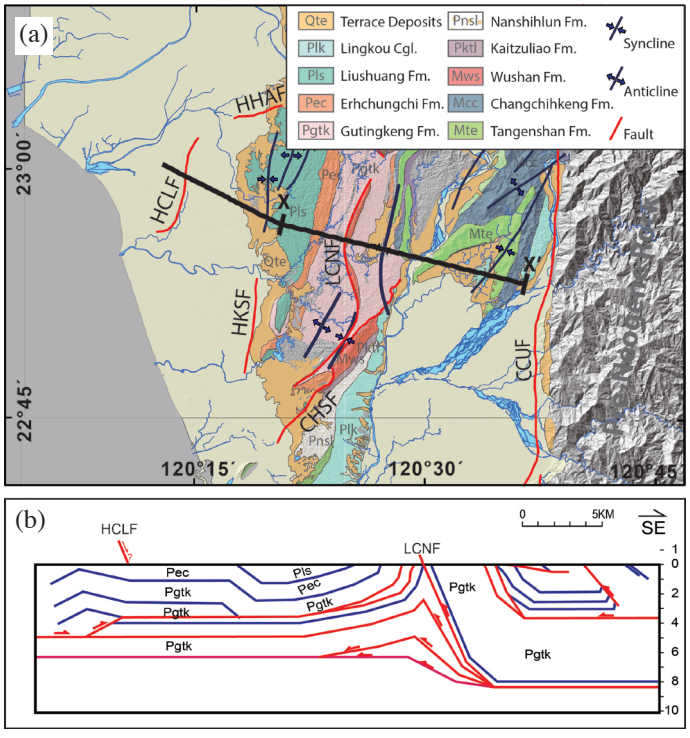

Fig. 3. (a) Geological backgrounds in southwestern Taiwan and (b) east-west seismic profile from Huang et al. (2004). Abbreviations: CCUF: Chaochu Fault; CHSF: Chishan Fault; LCNF: Lungchuan Fault; HCLF: Houchiali Fault; HHAF: HsinHua Fault; HKSF: HisaoKangshan Fault. (Color online only)

parts: (1) preparing and organizing the data in one-day data files from each station; (2) obtaining the cross-correlation functions (CCFs) by cross-correlation for each station pair (Bensen et al. 2007; Seats et al. 2012); (3) extracting the empirical Green's function (EGF) by stacking the cross-correlation functions for each station pair, (3) measuring the group and phase velocities as a function of frequency for Rayleigh wave dispersion from the EGF (Levshin and Lander 1989); and (4) jointly inverting the dispersion curves to obtain the three-dimensional S-wave velocity model (Fang et al. 2015). The procedures and methodology can be found in Fang et al. (2015) and Chen et al. (2016), respectively, in more detail.

There are three features in the three-dimensional S-wave inversion method of Fang et al. (2015), which are different from the traditional approach: (1) the depth sensitivity kernel, which is the partial derivative of the surface wave velocities, uses S-wave velocity as a function of depth to constrain the depth direction. This kind of direct inversion scheme is more straightforward than the traditional two-step scheme. (2) Wavelet-based sparsely-constrained tomography is the flexible regularization based on ray densities. (3) 2D ray tracing, fast marching method (Rawlinson and Sambridge 2004), is taken into account, which is applied to deal with ray bending in an inhomogeneous medium for each ray in different periods.

4. RESULTS

After cross-correlating the data and stacking all of the CCFs for each station pair, we obtained the EGFs for Rayleigh waves that display dispersion on the waveforms (Fig. 4a). Based on previous studies, the longest measurable period for station pairs depends on its interstation distance, which should be at least 2.5 times larger than the wavelength (e.g., Bensen et al. 2007; Lin et al. 2009; Porritt et al. 2011; Mordret et al. 2013). Because of this, we measured the dispersion curves over a period ranging from 0.6 - 5 s and the numbers of rays with longer periods decrease significantly (Figs. 4b and c). According to the ray path figures from different periods, the periods from 0.6 - 3.6 s cover most of the study region. The velocity patterns from different periods all show lower velocities toward the west (Fig. 5).

Before real data inversion, we performed the checkerboard tests in order to test the subsurface image robustness. We used 0.5 km grid size for inversion and performed checkerboard tests by alternatively assigning 20% positive and negative S-wave velocity anomalies to adjacent grids using grid sizes 4 km × 4 km × 1 km depth in the upper 1 km and 4 km × 4 km × 2 km to the base of the model. These checkerboard tests show that the shallow structure is well resolved from 0 - 4 km depths in the study region. The structure from 4 - 6 km depths is resolved in the southern part of the study region (Fig. 6). Therefore, based on the resolution test results, we only interpret features with dimensions larger than 4 km × 4 km and 1 km in the horizontal and vertical, respectively.

As a result, in the east-west vertical cross-sections from real data inversion, a low velocity zone is observed to the west of the seismic array in profiles A to C (Fig. 7). The lower velocity values occur in profile B and this low velocity zone is limited to around 2 - 3 km at depth. On the other hand, a high velocity zone can be observed east of the seismic array toward the mountain belt, which is related to exhumed metamorphic rocks. According to the checkerboard test results across profiles A to C, the dimension/length of the velocity anomalies from real data inversion are larger than the resolvable dimension/length (4 × 4 × 1 km) from the resolution tests, which indicates that those structures are reliable.

5. DISCUSSION AND CONCLUSIONS

As described in the Introduction section, the up-down displacement pattern from the InSAR results (Huang et al. 2016) show that the uplift region is limited in the Liushuang (Pls), Erhchungchi (Pec), and Gutingkeng (Pgtk) Formations (Figs. 3 and 8a). Those formations are interbeded with mudstone, sandstone and shale. The shallow structure at 0 - 1.5 km depths shows that the relatively low velocity region is right beneath the uplift region (Figs. 8 and 9). However, it should be mentioned that due to the deployment dimension of this temporary seismic array the actual relatively low velocity region may not be limited to this region, especially toward the west of the region. It deserves further investigation with another dense seismic array deployment to resolve the high-resolution shallow tomography. The large peak ground acceleration (PGA) values (> 400 gal) from TSMIP and S13 seismic networks were recorded in the same region (Fig. 1b). This could indicate that the shallow structure plays an important role for the coseismic displacement. GPS and leveling data from 2000 - 2010 have shown a similar uplift pattern as the coseismic pattern from the InSAR results and the uplift rate from GPS and leveling data can be up to 20 mm yr^{-1} in this region (Ching and Chen 2015). Ching and Chen (2015) and Huang et al. (2016) suggested that the deformation pattern could be controlled by high pore fluid pressure within the Pls, Pec, and Pgtk Formations and a relic onshore mud diapir beneath those formations. Huang et al. (2016) argued that the high pore fluid pressure region plays an important role in the dynamic stress changes that trigger this coseismic deformration. The Pls, Pec, and Pgtk Formations do not accumulate strain due to soft materials (mudstone) and can be easily deformed once forces are applied to the region.

Figures 9b and c show the ambient noise tomography results are compatible with those from a study by Huang et al. (2004) based on seismic reflection, surface geology and well data. The anticline and syncline structures observed

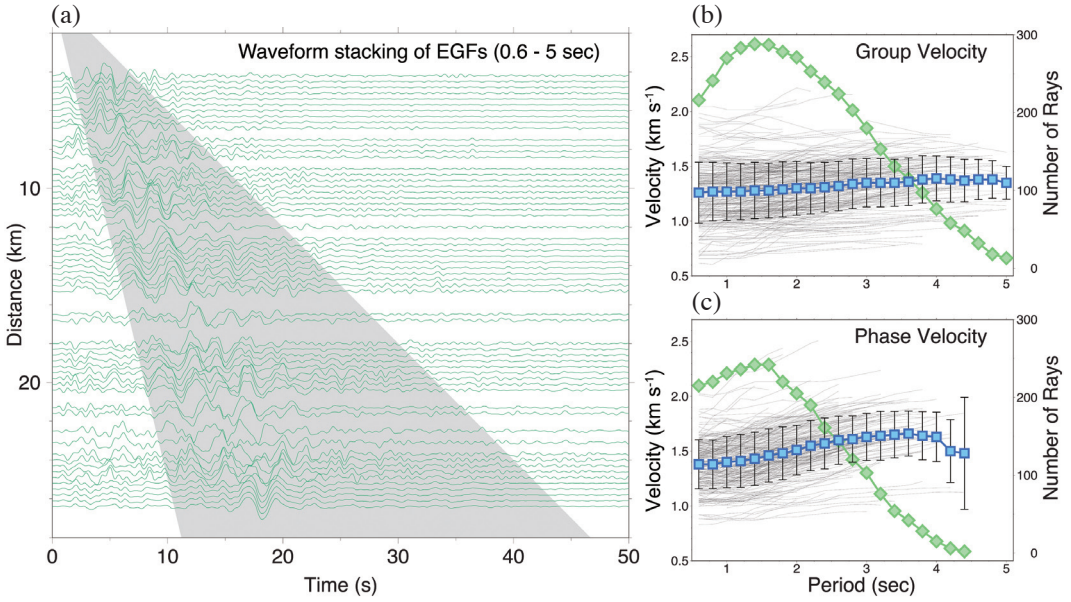

Fig. 4. (a) Waveform stacking of CCFs for each station pairs with 0.6 - 5 s period band filtered and sorted by interstation distance. Gray area shows the velocity ranges from 0.6 - 2.5 km s^{-1}. (b) Rayleigh wave group velocity. (c) Rayleigh wave phase velocity. In (b) and (c) panels, black curves represent the dispersion curves as a function of period while the blue squares are the averaged measurements with the associated standard deviation. The number of measurements for each period is shown in the green squares. (Color online only)

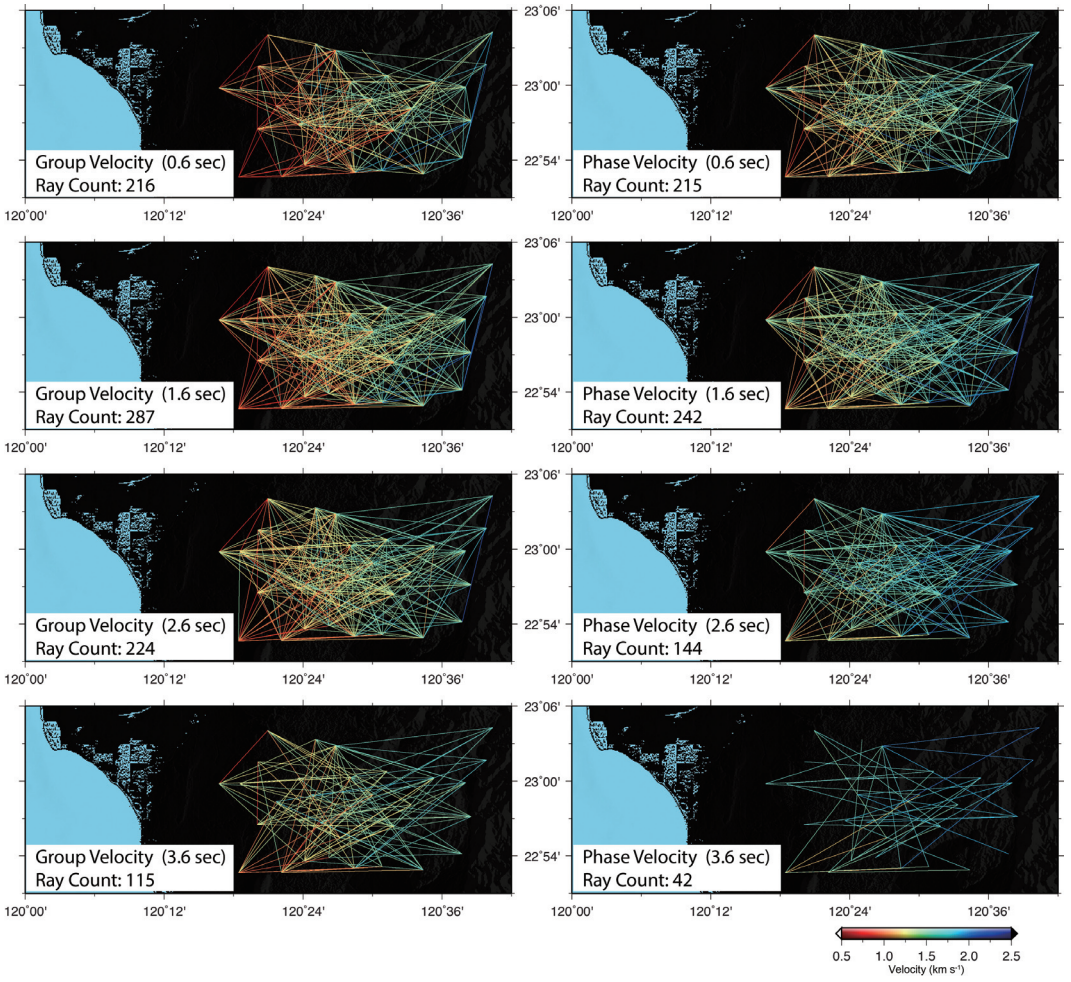

Fig. 5. Examples of the group and phase ray path velocities for Rayleigh waves from 0.6 - 3.6 s periods. (Color online only)

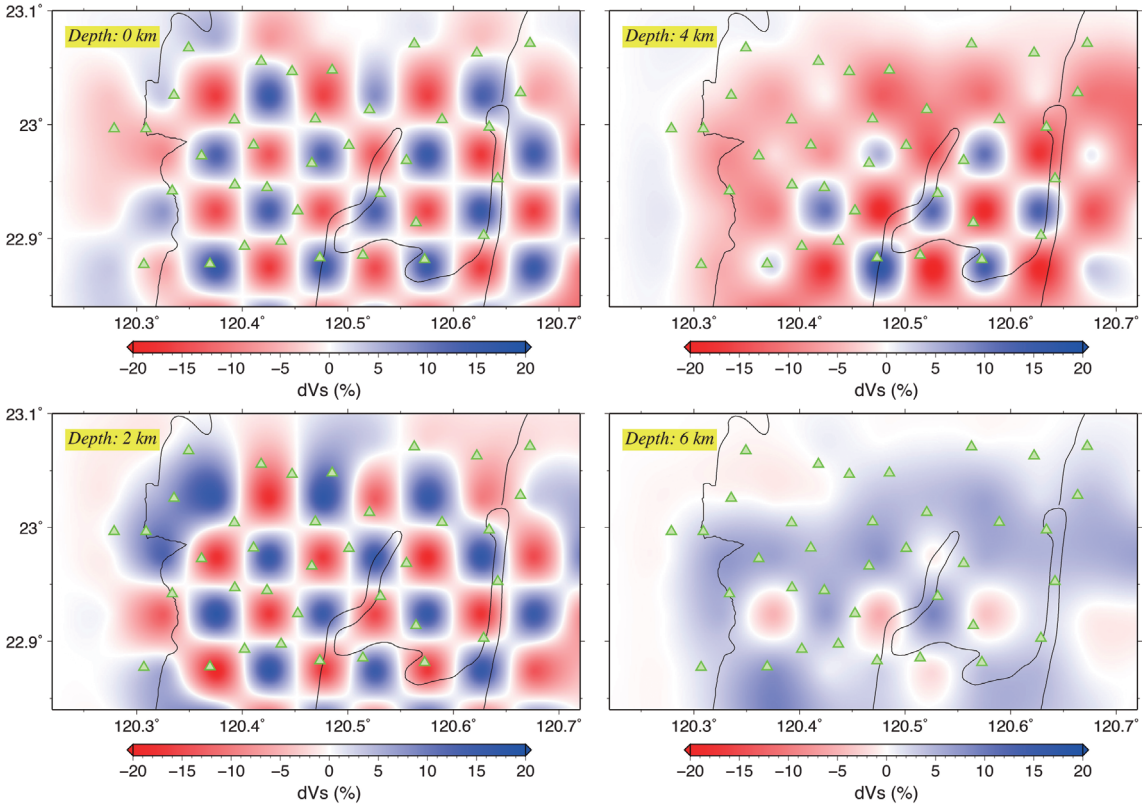

Fig. 6. The checkerboard test results at 0, 2, 4, and 6 km depths. (Color online only)

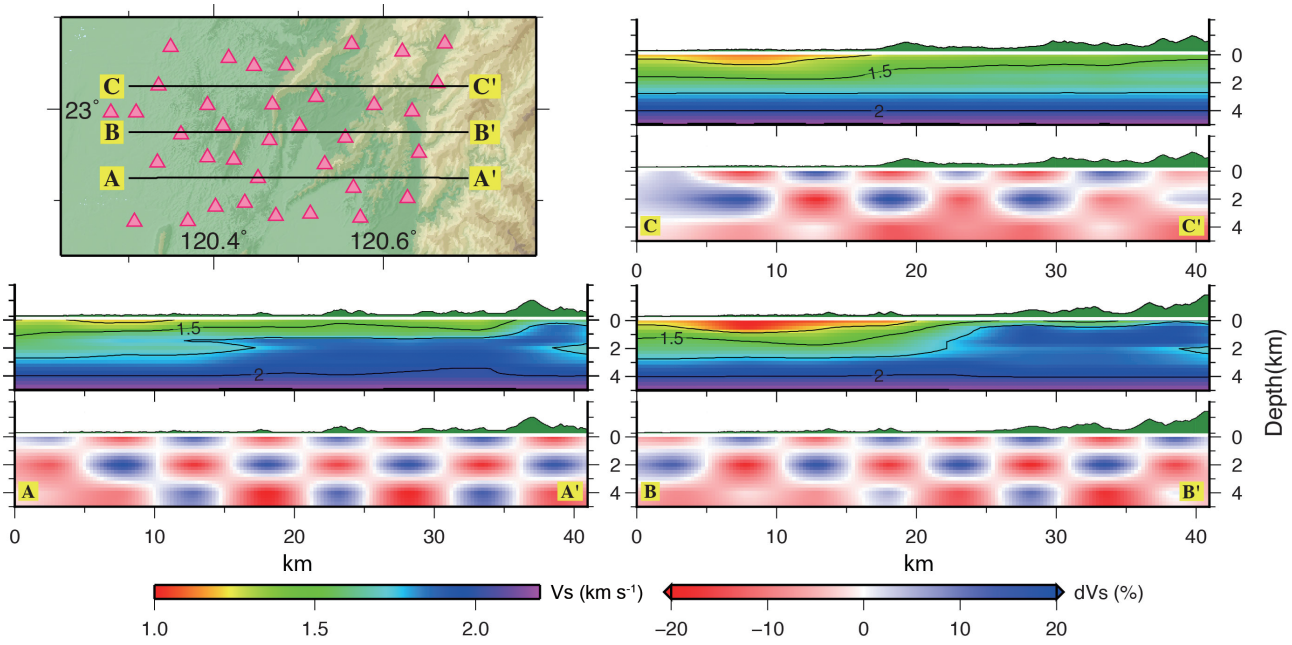

Fig. 7. Three vertical sections of the Vs model and their checkerboard tests. Top left panel: location of three sections. Bottom left panels: Vs model and checkerboard test of section AA'. Bottom right panels: Vs model and checkerboard test of section BB'. Top right panels: Vs model and checkerboard test of section CC'. (Color online only)

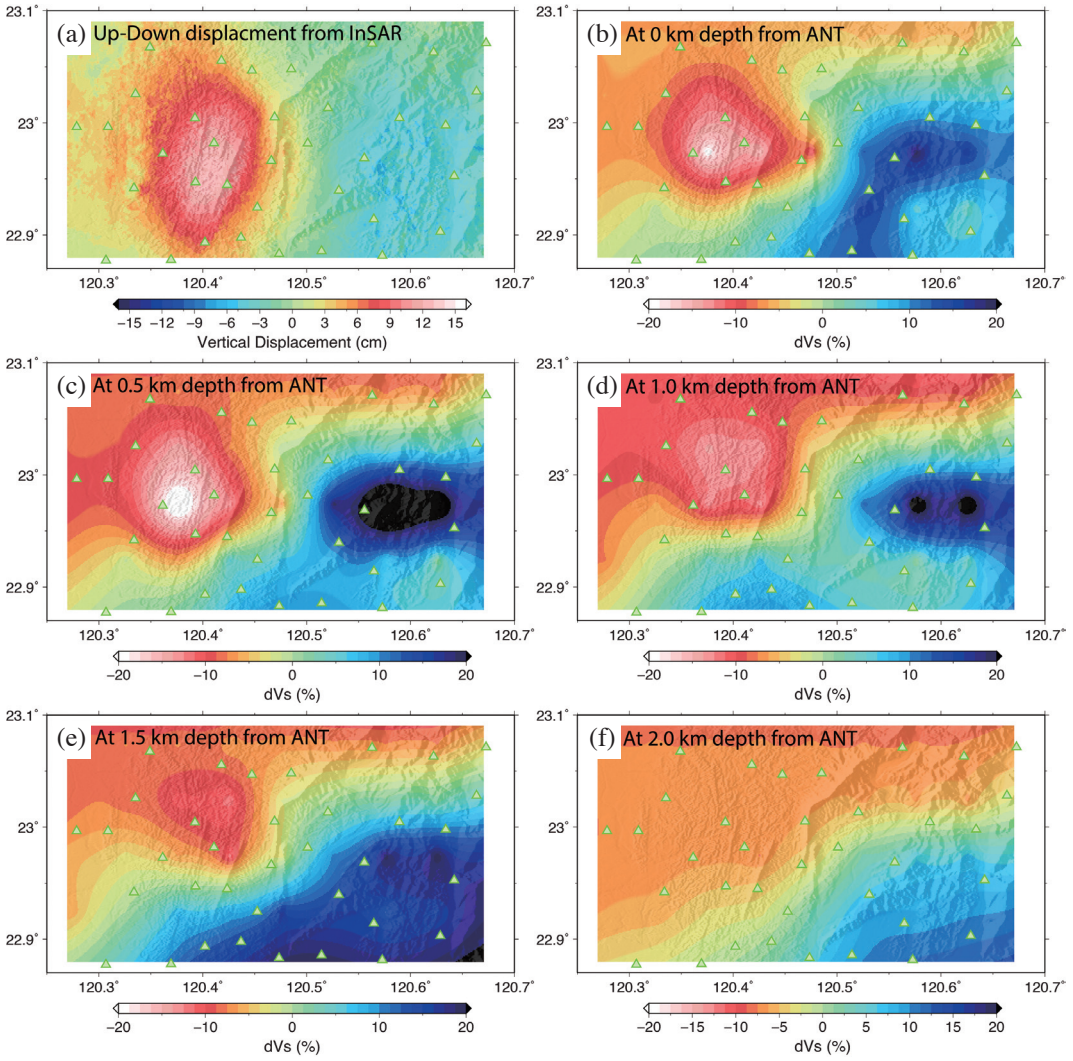

Fig. 8. (a) The vertical coseismic displacement from InSAR results (Huang et al. 2016). (b) to (f) The horizontal slices of the Vs perturbation model (dVs) from 0 - 2 km depths. (Color online only)

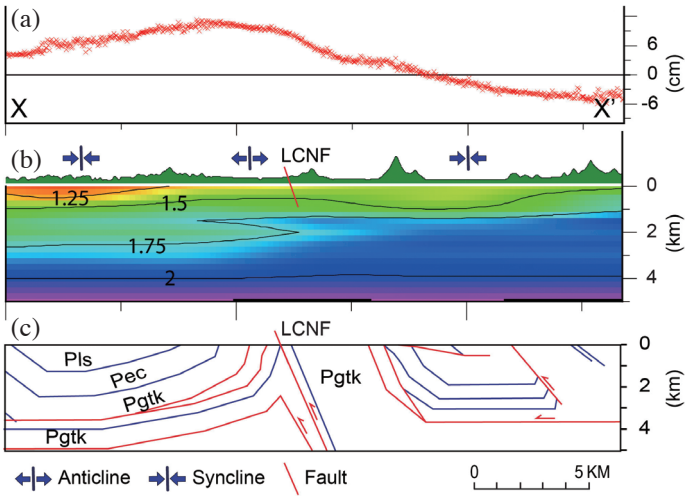

Fig. 9. The XX' vertical section of (a) up-down displacement from InSAR (Huang et al. 2016), (b) Vs model in this study, and (c) interpretation of seismic profile from Huang et al. (2004). The Vs model contour patterns are similar to the seismic profile interpretation from Huang et al. (2004). See Fig. 3 for the XX' section location. (Color online only)

from the surface geology and from Huang et al. (2004) also reveal these results. We further compared our results with previous studies (Kuo-Chen et al. 2012; Huang et al. 2014) in this region using different data sets and methods. Kuo-Chen et al. (2012) used TAIGER (Taiwan Geodynamic Research project) seismic data and broadband seismic data from the Central Weather Bureau for inverting Vs tomography. Huang et al. (2014) used well logging data, TSMIP, and S13 data from the Central Weather Bureau in addition to the data set of Kuo-Chen et al. (2012). In terms of methodology, previous studies and this study used travel time data from body waves and from surface waves to invert Vs structure, respectively. With dense seismic stations and travel time data from surface waves in this study, we were able to obtain finer shallow structure in this region (Fig. 10). As shown in Fig. 10, the shallow structure improved with more data sets from Kuo-Chen et al. (2012) to Huang et al. (2014) and the structure got better from Huang et al. (2014) to this study because of the dense array data and ambient noise tomography used in this study. This temporary seismic network has demonstrated that with dense seismic array deployment we can obtain the shallow velocity structure from the ambient noise, especially S waves, with high resolution.

Acknowledgements This project is supported by the Ministry of Science and Technology (Grant No.: MOST 104-2628-M-008-005-MY3 and MOST 106-2119-M-008-006). Discussion with Dr. J.-Y. Yen of National Dong Hwa University is appreciated. Thanks to Dr. M.-H. Huang of the Jet Propulsion Laboratory (JPL), Caltech for providing the InSAR results. We also thank Dr. Yao of USTC for providing the ambient noise tomography codes.

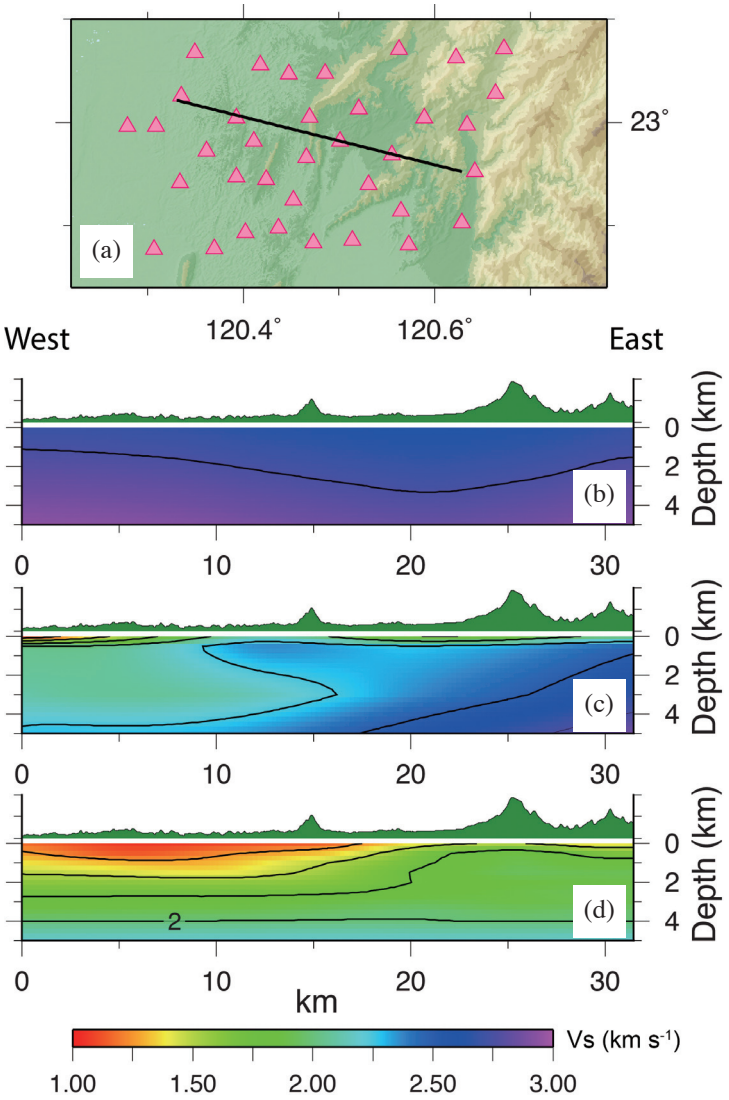

Fig. 10. The tomographic result from this study compared with previous studies (Kuo-Chen et al. 2012; Huang et al. 2014). (a) Map view of the section of (b) to (c). Pink triangle: seismic station. Solid line: the location of the section. (b) Vs section from Kuo-Chen et al. (2012). (c) Vs section from Huang et al. (2014). (d) Vs section from this study. (Color online only)

REFERENCES

Bensen, G. D., M. H. Ritzwoller, M. P. Barmin, A. L. Levshin, F. Lin, M. P. Moschetti, N. M. Shapiro, and Y. Yang, 2007: Processing seismic ambient noise data to obtain reliable broad-band surface wave dispersion measurements. *Geophys. J. Int.*, **169**, 1239-1260, doi: 10.1111/j.1365-246X.2007.03374.x. [Link]

Chen, K. X., H. Kuo-Chen, D. Brown, Q. Li, Z. Ye, W. T. Liang, C. Y. Wang, and H. Yao, 2016: Three-dimensional ambient noise tomography across the Taiwan Strait: The structure of a magma-poor rifted margin. *Tectonics*, **35**, doi: 10.1002/2015TC004097. [Link]

Ching, K. E. and K. H. Chen, 2015: Tectonic effect for establishing a semi-dynamic datum in Southwest Taiwan. *Earth Planets Space*, **67**, doi: 10.1186/s40623-015-0374-0. [Link]

Fang, H., H. Yao, H. Zhang, Y. C. Huang, and R. D. Van Der Hilst, 2015: Direct inversion of surface wave dispersion for 3-D shallow crustal structure based on ray tracing: Methodology and application. *Geophys. J. Int.*, **201**, 1251-1263, doi: 10.1093/gji/ggv080. [Link]

Ho, C. S., 1986: An Introduction to the Geology of Taiwan: Explanatory Text of the Geologic Map of Taiwan, Central Geological Survey, MOEA, Taipei, ROC, 163 pp. (in Chinese)

Huang, H. H., Y. M. Wu, X. Song, C. H. Chang, S. J. Lee, T. M. Chang, and H. H. Hsieh, 2014: Joint Vp and Vs tomography of Taiwan: Implications for subduction-collision orogeny. *Earth Planet. Sci. Lett.*, **392**, 177-191, doi: 10.1016/j.epsl.2014.02.026. [Link]

Huang, M. H., H. Tung, E. Fielding, H. H. Huang, C. Liang, C. Huang, and J. C. Hu, 2016: Multiple fault slip triggered above the 2016 Mw 6.4 Meinong earthquake in Taiwan. *Geophys. Res. Lett.*, **43**, doi: 10.1002/2016GL069351. [Link]

Huang, S. T., K. M. Yang, J. H. Hung, J. C. Wu, H, H, Ting, W. W. Mei, S. H. Hsu, and M. Lee, 2004: Deformation front development at the northeast margin of the Tainan basin, Tainan-Kaohsiung area, Taiwan. *Mar. Geophys. Res.*, **25**, 139-156, doi: 10.1007/s11001-005-0739-z. [Link]

Kuo-Chen, H., F. T. Wu, and S. W. Roecker, 2012: Three-dimensional P velocity structures of the lithosphere beneath Taiwan from the analysis of TAIGER and related seismic data sets. *J. Geophys. Res.*, **117**, B06306, doi: 10.1029/2011JB009108. [Link]

Levshin, A. L. and A. V. Lander, 1989: Recording, identification and measurement of surface wave parameters. In: Keilis-Borok, V. I. (Ed.), Seismic Surface Waves in a Laterally Inhomogeneous Earth, Kluwer Acad., Dordrecht, Netherlands, 131-182, doi: 10.1007/978-94-009-0883-3_5. [Link]

Lin, F. C., M. H. Ritzwoller, and R. Sneider, 2009: Eikonal tomography: Surface wave tomography by phase front tracking across a regional broadband seismic array. *Geophys. J. Int.*, **177**, 1091-1110, doi: 10.1111/j.1365-246X.2009.04105.x. [Link]

Mordret, A., N. M. Shapiro, S. Singh, P. Roux, and O. I. Barkved, 2013: Helmholtz tomography of ambient noise surface wave data to estimate Scholte wave phase velocity at Valhall life of the field. *Geophysics*, **78**, WA99-WA109, doi: 10.1190/geo2012-0303.1. [Link]

Porritt, R. W., R. M. Allen, D. C. Boyarko, and M. R. Brudzinski, 2011: Investigation of Cascadia segmentation with ambient noise tomography. *Earth Planet. Sci. Lett.*, **309**, 67-76, doi: 10.1016/j.epsl.2011.06.026. [Link]

Rawlinson, N. and M. Sambridge, 2004: Wave front evolution in strongly heterogeneous layered media using the fast marching method. *Geophys. J. Int.*, **156**, 631-647, doi: 10.1111/j.1365-246X.2004.02153.x. [Link]

Seats, K. J., J. F. Lawrence, and G. A. Prieto, 2012: Improved ambient noise correlation functions using Welch's method. *Geophys. J. Int.*, **188**, 513-523, doi: 10.1111/229j.1365-246X.2011.05263.x. [Link]

Teng, L. S., 1987: Stratigraphic records of the late Cenozoic Penglai orogeny of Taiwan. *Acta Geol. Taiwan*, **25**, 205-224.